CONSTITUTIVE MODELING OF LASER SHOCK PEENING ON ADDITIVE MANUFACTURED Ti–6Al–4V

A Dissertation

Presented to the Faculty of the Graduate School

of Cornell University

In Partial Fulfillment of the Requirements for the Degree of

Master of Science

by

Ruidong Wang

May 2021

ABSTRACT

Ruidong Wang

Laser shock peening (LSP) is a mechanical surface treatment that induces plastic deformation and compressive residual stress in the material similar to shot peening. Pressure generated by the pulsed laser is far above the yield stress of the material and pulse duration is on the order of nanosecond. Finite element analysis is applied to simulate LSP and predict plastic deformation and residual stress through different constitutive models. The development of analytical model including model details, loading time history and constitutive model equations and parameters is discussed. Finally, results are presented for different constitutive models and experiment results are discussed.

BIOGRAPHICAL SKETCH

Ruidong Wang is currently a 2nd year M.S. student in the material science and engineering department at Cornell University. In May 2021, he will graduate with a M.S. degree. He graduated from Qingdao No.2 high school in June 2014 and finished his B.S. degree in chemical engineering at University of California San Diego. During his undergraduate study, He joined many research groups and practiced in chemical synthesis labs including Zheng Chen's lab in UCSD, Xuhong Guo's lab at East China University of Science and Technology and Qiong Zhou's lab in China University of Petroleum. In his master study, he joined Atieh Moridi's lab focusing on additive manufacturing and surface treatments. This experience helped him to understand material properties better and trained him on material characterization techniques as well as simulation techniques.

ACKNOWLEDGEMENTS

I would like to express my appreciation to my committee chair, Professor Atieh Moridi who always gave me guidance when I was lost and who encouraged me with her enthusiasm. She helped me to stay on track and kept me engaged in the research. It was an enjoyable experience working with her and this thesis would not have been possible without her help and guidance.

I would also like to appreciate my committee member Professor Mostafa Hassani who helped me greatly on simulations with his knowledge on the subject. When I ask him about my confusions, he always explains everything clearly and communication with him is a pleasure.

Lastly, I would like to thank Jenniffer Bustillos and Jinyeon Kim for their time and help on my experiments. Experiments would not go so smoothly without their help.

TABLE OF CONTENTS

LIST OF TABLES

LIST OF FIGURES

1. Introduction

To minimize loss due to structure failures, technologies to prolong component lifetime has become a popular research area. Many surface treatments were developed to reduce tensile stress caused by cyclic loading to further prevent the initiation of fatigue cracks and laser shock peening (LSP) is one of mechanical surface treatment. In LSP, a high energy pulsed laser beam is directed towards the surface of metal subject possibly coated with an absorbent layer and covered with a transparent overlay as shown in figure.1. When laser beam hits the metal surface, it generates a high energy plasma which creates a shock wave that propagates into the metal. As a result, compressive residual stresses are generated due to shock wave induced plastic deformation in the metal [5]–[8]. Furthermore, the presence of compressive residual stress improves mechanical properties, fatigue life, corrosion resistance and wear resistance of material[4], [9], [10].

Because of the complex physics behind LSP and difficulty of measurement, accurate modeling of LSP has become an active research area. Berthe et al [11] studied the pressure generated in LSP process and created an analytical model based on laser power density. Wu et al [12] proposed a new non-linear relationship between the shock pressure and particle velocity and created a more complex model for LSP pressure profile. Based on these fundamental understanding of LSP, experiments and investigations of LSP on different materials and under different conditions were conducted[13], [14].

Finite Element modeling (FEM) was first introduced by Braisted and Brockman in 1999 to study the residual stress and mechanical behavior of Ti6Al4V using Abaqus software[15]. Since then, various FE algorithms and models for LSP were proposed [16]–[18]. However, discrepancies between experimental and simulation results still exist because some parameters used in simulation were not precise enough for an accurate simulation and no standard simulation process or parameters are established for LSP yet. Therefore, developing a reliable and accurate model for LSP is both challenging and important.

This paper will examine different LSP parameters including pressure profile, spatial profile and temporal profile as well as different material models. Experimental results will be used to validate these parameters and models and thus the capability of each model can be determined. Furthermore, optimized model parameters can be obtained through curve fitting.

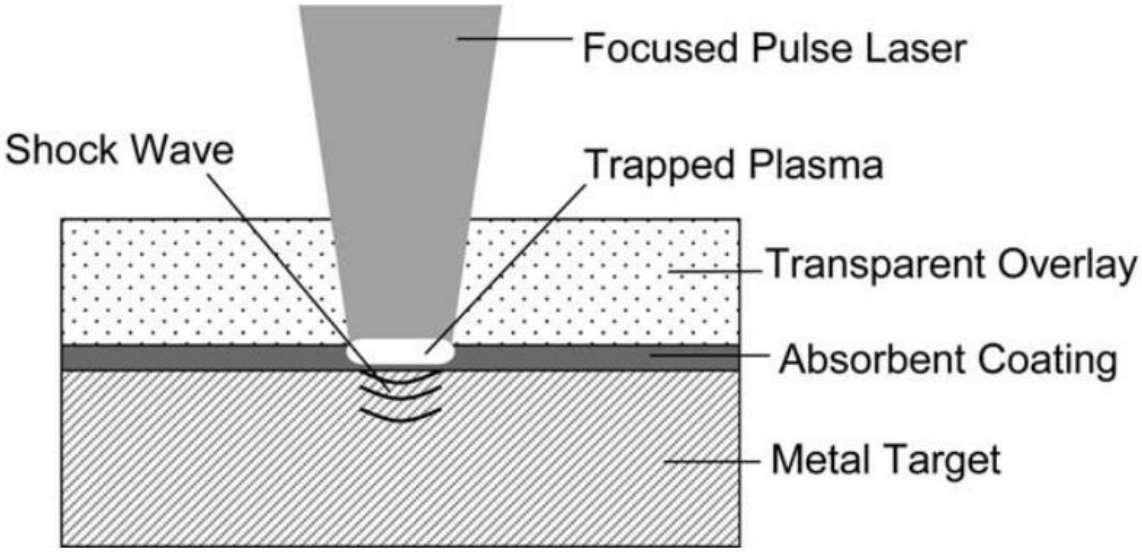

Figure 1: Schematic diagram of laser shock peening [4]

2. Material models details and material parameters

In this paper, Ti–6Al–4V is used to investigate LSP process and its material properties are listed in Table.1. In LSP process, strain rate goes up to 10^6/s and material behavior changes significantly under such high strain rate compared to that under quasi-static loading [19]. Many material models were proposed to model the plastic behavior of materials including elastic perfectly plastic (EPP) model, Johnson and cook (JC) model, Zerilli and Armstrong (ZA) model, Khan-Huang-Liang (KHL) model and etc. In this paper, we will focus on EPP, JC and ZA models and detailed parameters selected for each model are summarized in Table 2.

Table.1 Material properties of Ti–6Al–4V.

Property	Value
Young's modulus (GPa)	113.8
Poisson's ratio	0.342
Density (kg m^{-3})	4500
Hugoniot elastic limit (MPa)	2800
Specific heat (J/kg)	560
Thermal conductivity (W/(m K))	7
Hugoniot elastic limit (GPa)	2.8

Table.2 Model parameters for each material model

JC parameters		Reference	ZA parameters		Reference
A(MPa)	997.9	[1]	C_0(MPa)	340	[2]
B(MPa)	653.1	[1]	B_0(MPa)	1135	[2]
n	0.45	[1]	B(MPa)	1485	[2]
C	0.0198	[1]	C_n	0.5	[2]
m	0.7	[1]	$\alpha_0(K^{-1})$	1.4×10^{-5}	[2]
T_m(K)	1941	[1]	$\alpha_1(K^{-1})$	7×10^{-5}	[2]
			$\beta_0(K^{-1})$	2.75×10^{-3}	[2]
			$\beta_1(K^{-1})$	7.47×10^{-5}	[2]

Enhanced ZA parameters		Reference
C_0(MPa)	472.5981	[3]
B_0(MPa)	2221.873	[3]
B(MPa)	247.1272	[3]
ε_r	0.0308	[3]
$\alpha_0(K^{-1})$	1×10^{-6}	[3]
$\alpha_1(K^{-1})$	1.849×10^{-4}	[3]
$\beta_0(K^{-1})$	1.16×10^{-6}	[3]
$\beta_1(K^{-1})$	0.16	[3]

Table.2 Model parameters for each material model

JC parameters		Reference	ZA parameters		Reference
A(MPa)	997.9	[1]	C_0(MPa)	340	[2]
B(MPa)	653.1	[1]	B_0(MPa)	1135	[2]
n	0.45	[1]	B(MPa)	1485	[2]
C	0.0198	[1]	C_n	0.5	[2]
m	0.7	[1]	$\alpha_0(K^{-1})$	1.4×10^{-5}	[2]
T_m(K)	1941	[1]	$\alpha_1(K^{-1})$	7×10^{-5}	[2]
			$\beta_0(K^{-1})$	2.75×10^{-3}	[2]
			$\beta_1(K^{-1})$	7.47×10^{-5}	[2]

Enhanced ZA parameters		Reference
C_0(MPa)	472.5981	[3]
B_0(MPa)	2221.873	[3]
B(MPa)	247.1272	[3]

ε_r	0.0308	[3]
$\alpha_0(K^{-1})$	1×10^{-6}	[3]
$\alpha_1(K^{-1})$	1.849×10^{-4}	[3]
$\beta_0(K^{-1})$	1.16×10^{-6}	[3]
$\beta_1(K^{-1})$	0.16	[3]

2.1 EPP model

EPP model is the simplest model among all these models because no strain hardening or strain rate dependence is considered and material is assumed to be perfectly plastic after yield occurs. Therefore, stress remains constant after yield stress is reached. The yield stress is calculated based on Hugoniot elastic limit (HEL). HEL is defined as the point at which a material transitions from purely elastic state to a elastic-plastic state. Therefore, when stress reaches HEL, the material is assumed to yield at this point. The relationship between yield stress (σ_y) and HEL is shown as Eq.1:

$$\sigma_y = HEL\frac{1-2\nu}{1-\nu}$$

Where ν is Poisson's ratio. This model only requires minimum data input and it does not take temperature, strain and strain rate into consideration.

2.2 JC model

JC model is widely used to model process with high strain rate. Flow stress (σ) in JC model is determined by the multiplication of three parts: strain hardening part, strain rate dependent part and temperature part as shown in Eq.2:

$$\sigma = [A + B\varepsilon^n]\left[1 + C\ln\frac{\dot{\varepsilon}}{\dot{\varepsilon}_0}\right][1 - T'^m]$$

Where A, B, n, C and m are constants. ε and $\dot{\varepsilon}$ are strain and strain rate respectively. T' is non-dimensionalized temperature:

$$T' = \frac{T - T_r}{T_m - T_r}$$

where T_r and T_m are room temperature and melting temperature of material respectively. Parameter A is material yield strength in room temperature. Parameter B and n are strain hardening constants. Parameter C is strain rate sensitivity constant and parameter m is thermal softening exponent.

2.3 ZA model

Like JC model, ZA model has also successfully modeled material deformation at high strain rate [20]. ZA model is based on dislocation motions of plastic deformation and therefore, each material structure type (face-centered cubic (FCC), body-centered cubic (BCC) and hexagonal close packed (HCP)) has its own governing equation. For FCC metals, activation volume is strain dependent while for BCC metals, activation volume is not strain dependent [21]. Deformation response of HCP metals, on the other hand, is in between FCC metals and BCC metals [22]. Flow stress relationship for FCC metals and BCC metals are shown in Eq.3 and Eq.4 respectively:

$$\sigma = C_1 + C_5\varepsilon^n e^{-C_3T + C_4T\ln\dot{\varepsilon}}$$

$$\sigma = C_1 + C_2 e^{-C_3T + C_4T\ln\dot{\varepsilon}} + C_5\varepsilon^n$$

Where C_1, C_1, C_1, C_1, C_1 and n are constants. For HCP metals, flow stress relationship is the superposition of FCC and BCC equations:

$$\sigma = C_0 + B_0\varepsilon^{C_n} e^{-\alpha_0T + \alpha_1T\ln\dot{\varepsilon}} + Be^{-\beta_0T + \beta_1T\ln\dot{\varepsilon}}$$

Where C_0, B_0, B, α_0, α_1, β_0, β_1 and C_n are material constants. ε, $\dot{\varepsilon}$ and T are strain, strain rate and temperature respectively.

2.4 Enhanced ZA model

Some paper reported a model that is similar to ZA model but without temperature dependence because LSP is a mechanical surface treatment [3], [23]. However, laser shock peening is not a process that is completely temperature independent. Warm laser shock peening (WLSP) which is laser shock peening of a pre-warmed subject has shown its ability to further enhance material mechanical properties [24]. The capacity of ZA model with and without temperature dependence will be compared in this paper.

Flow stress relationship for FCC, BCC and HCP metals without temperature dependence are shown as Eq.6, Eq.7 and Eq.8 respectively:

$$\sigma = C_1 + C_5\varepsilon^n e^{-C_3+C_4 \ln \dot{\varepsilon}}$$

$$\sigma = C_1 + C_2 e^{-C_3+C_4 \ln \dot{\varepsilon}} + C_5\varepsilon^n$$

$$\sigma = C_0 + B_0\sqrt{\varepsilon_r(1 - e^{\frac{-\varepsilon}{\varepsilon_r}})}\, e^{-\alpha_0+\alpha_1 \ln \dot{\varepsilon}} + Be^{-\beta_0+\beta_1 \ln \dot{\varepsilon}}$$

all the parameters represent the same meaning as explained in ZA model and new parameter ε_r is a material constant that need to be determined.

3. Simulation procedure

In this paper, Abaqus[25] software was used to perform finite element analysis of LSP process and Fig.2 is a representation of simulation model. CAX4R (continuum axi-symmetric 4 noded reduced integration) elements are used through the entire model which is a 36 mm × 36 mm square. Area of interest at the top left corner is a 6 mm × 6 mm square and axisymmetric boundary condition is applied at the left edge of the model. To accurately model the impact of LSP, a mesh size of 0.01 mm × 0.01 mm is used at area of interest and mesh size gradually increase from 0.01 mm to 0.1 mm at coarser mesh region.

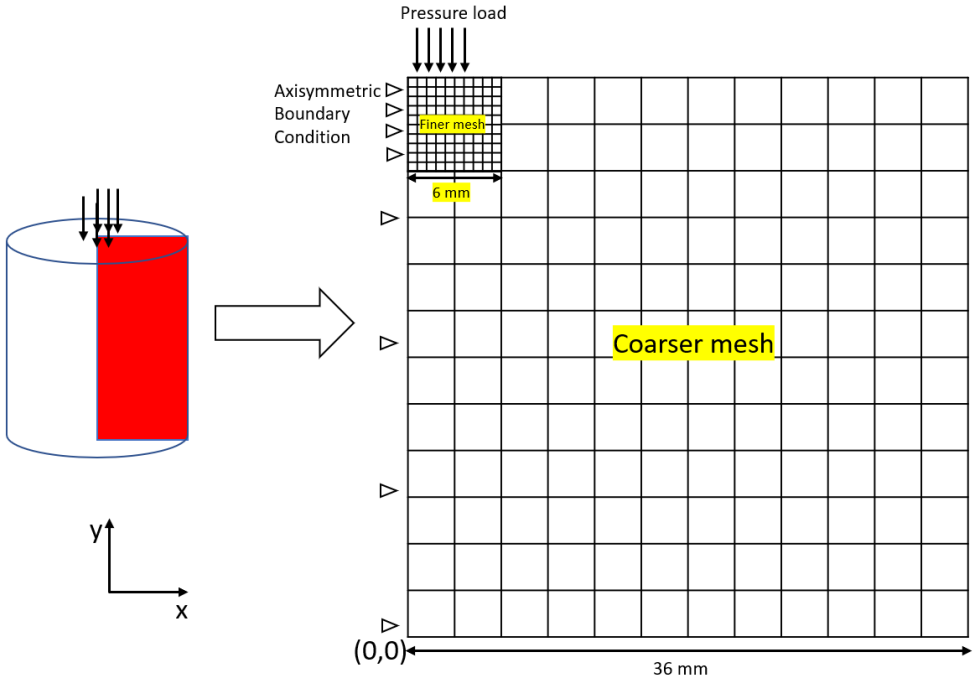

Figure 2: Schematic diagram of FE model

3.1 pressure load

As shown in Fig.2, pressure load is applied at the top of the model from x=0 to x=4. The Spatial and temporal depends on the laser system. Various time profiles of pressure were used in literature including gaussian shape distribution[26], triangular shape distribution[15] and experiment determined distribution[27]. In this paper, a triangular ramp temporal profile is used as shown in Fig.3 and the spatial profile of pressure is assumed to be uniform.

Peak pressure of LSP process can be estimated through an equation [28]:

$$P(GPa) = 0.01\sqrt{\frac{\alpha}{2\alpha+3}}\sqrt{Z(g\ cm^{-2}s^{-1})}\sqrt{I_0(GW\ cm^{-2})}$$

$$\frac{2}{Z} = \frac{1}{Z_1} + \frac{1}{Z_2}$$

Where α is the efficiency factor which is determined by percent incident energy density that is used for pressure rise of plasma[29], Z is a reduced acoustic impedance of confining (Z_1) and target (Z_2) materials and I_0 is the power density of pulsed laser. The value of α ranges from 0.1-0.3 in literature [30], [31].

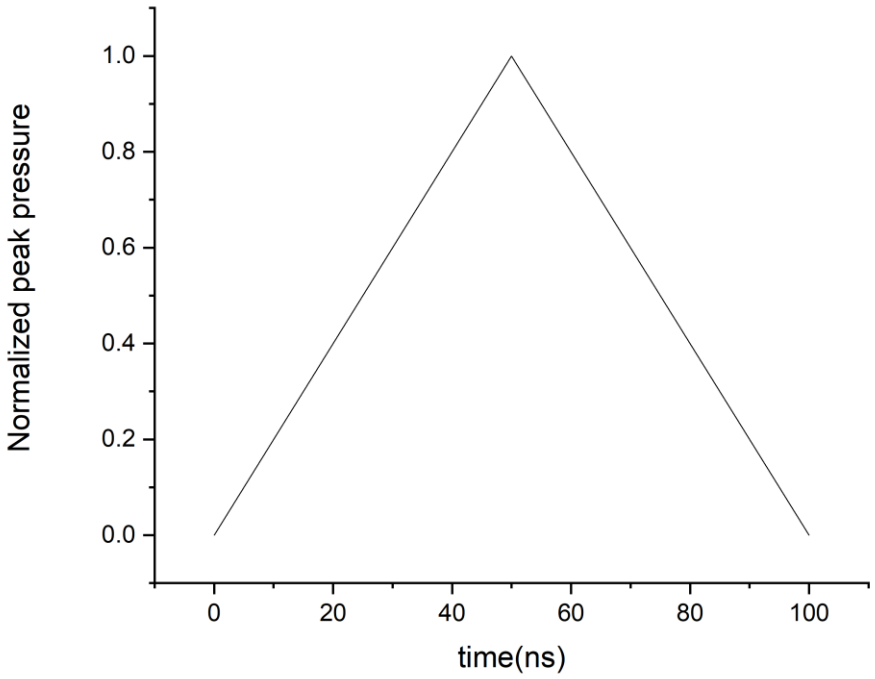

Fig.3: time profile of pressure

3.2 Analysis procedures

The simulation of LSP process can be described in two steps. First, the laser firing step, which features a very short interaction time as the shock waves travel through the material, is modeled and run in Abaqus/Explicit. Solution time for this step is usually at least two orders of magnitude longer than laser pulse duration to ensure the saturation of plastic deformation in the material [15].

Second, the recovery step, in which stable equilibrium occurs relatively slowly, is modeled and run in Abaqus/Standard. The data of stress and strain states in the first step were imported to the second step as

initial state and residual stress data can be obtained after the second step. If more than one shot is required, the stress and strain states of the second step will then be imported back to step one as initial states.

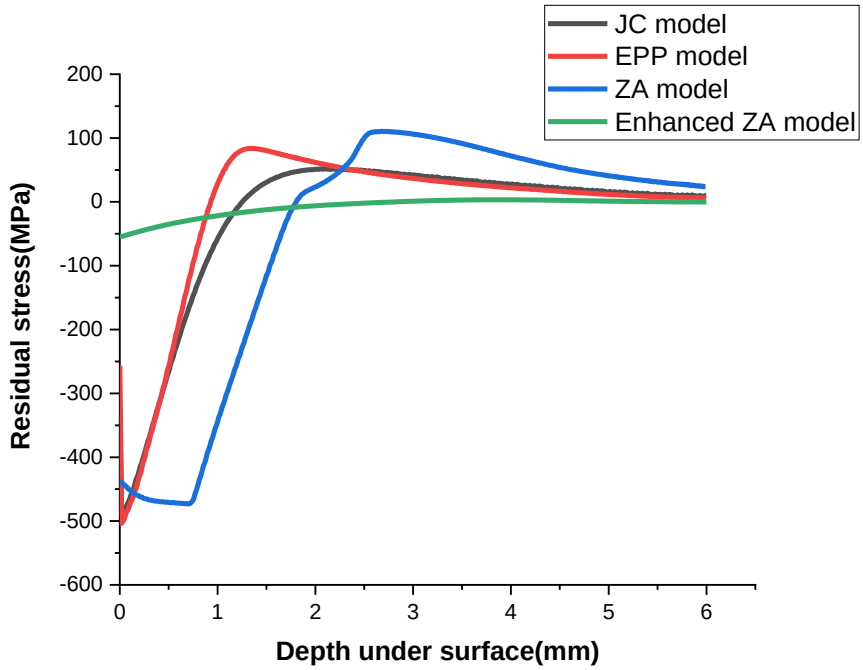

Fig.4: residual stress variation along depth at x=1.4mm and power density=7 $GW\ cm^{-2}$

4. Results and Discussions

Three power densities for LSP process are discussed in this work: 7 $GW\ cm^{-2}$, 8.5 $GW\ cm^{-2}$ and 10 $GW\ cm^{-2}$. The corresponding peak pressures for each power density are calculated to be 4.32GPa, 4.76GPa and 5.164GPa respectively with the value of α=0.3. 4 models are considered for each peak pressure. Fig.4 and Fig.5 shows the residual stress and PEEQ variations for all 4 models at 7 $GW\ cm^{-2}$.

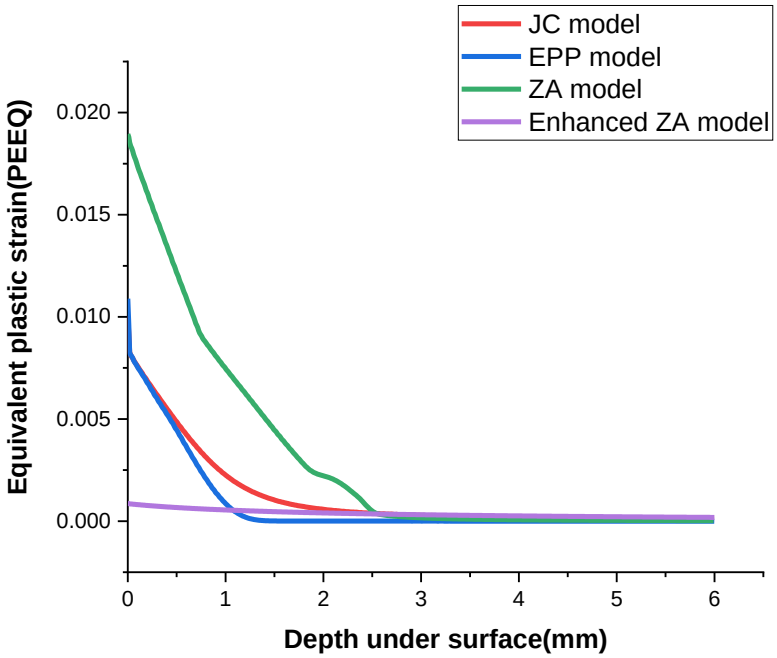

Fig.5: PEEQ variation along depth at x=1.4mm and power density=7 $GW\ cm^{-2}$

4.1 EPP model and JC model

Fig. 6(a) and Fig. 7(a) shows the residual stress versus depth below the surface curve for each power densities and Fig. 6(b) and Fig. 7(b) shows the equivalent plastic strain versus depth below the surface curve for each power densities. Data were collected at 1.4 mm away from the center of the laser shot. Plastic strains on the surface are the highest and gradually decrease with depth. This result agrees with the general trend that a pressure increase will result in a larger deformation. Also, we observed a decrease in residual stress in the near surface region in our simulations. Such phenomenon is also reported by other researchers and the reason is sharp decline of generated compressive wave near the surface during the contact time[23]. Given that residual stress values depend significantly on magnitude of the wave, a drop in residual stress near the surface is expected.

In Fig.4 and Fig.5, we can see that the residual stress values and PEEQ values obtained from JC model and EPP model are very similar. However, in EPP model, plastic strain decreased faster than that in JC

model. As shown in Fig. 6(b) and Fig. 7(b), both curves have a steep decrease from surface to a depth of around 1.5mm. In EPP model, plastic strain is roughly zero below 1.5mm under the surface but in JC model, plastic strain still remains at roughly 0.2%. This phenomenon results in a smaller overshoot of residual stress for JC model at depth 1.5mm to 2mm.

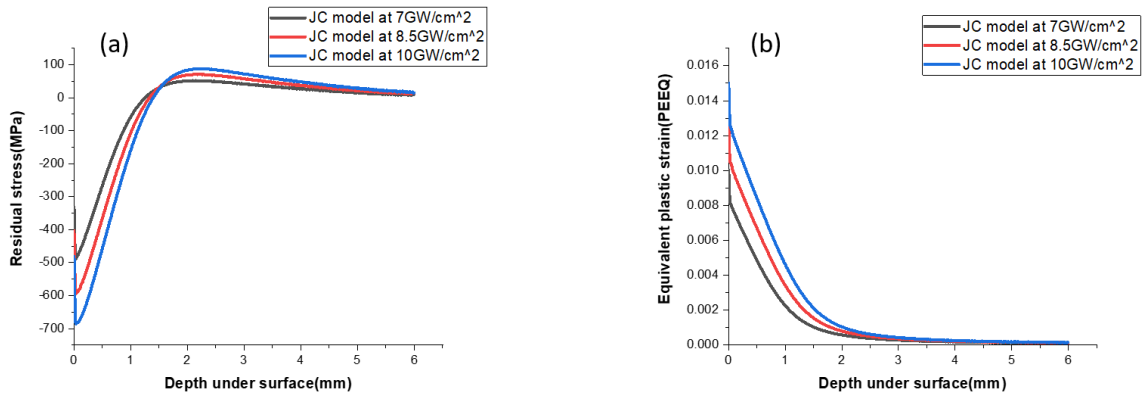

Fig.6: Simulation results for JC model on (a) residual stress (b) PEEQ

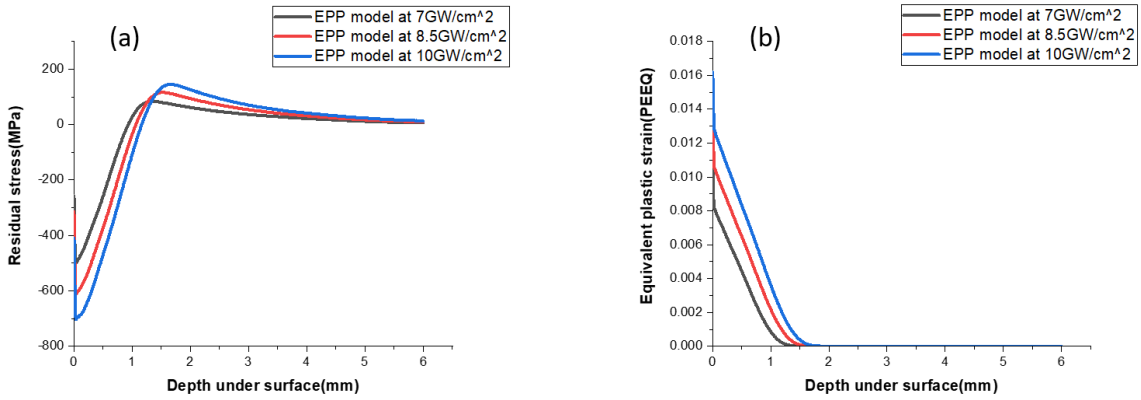

Fig.7: Simulation results for EPP model on (a) residual stress (b) PEEQ

4.2 ZA model

Fig. 8(a) and Fig. 8(b) shows the residual stress and equivalent plastic strain in ZA model versus depth below the surface curve for each power densities. In Fig. 8(b), we also observed the decreasing trend of plastic strain with respect to depth which means ZA model also successfully predicted the general trend. Also, as shown in Fig.5, plastic strain value in ZA model is the highest in all 4 models. However, higher plastic strain value in ZA model does not result in higher residual stress value near the surface as shown in Fig.4. Moreover, as shown in Fig. 8(a), residual stress values near the surface for all three power densities stayed roughly the same. The reason for such results can be explained through Fig.9 which is the time history for ZA model. The overall time history is shown in Fig. 9(a) and since pressure load is applied for the first 100ns of the simulation, we also plotted the undeveloped residual stress at 120ns<t<470ns as shown in Fig.9 (b). In Fig.9 (b), the trend of increasing residual stress as power density increased is observed. However, due to the complicated time history of ZA model, we are not able to see this trend after stress is completely developed. Although residual stress value near the surface does not increase with increasing power densities, we observed an overall increase in compressive residual stress. Depth of compressive residual stress increased from 1.8mm to 2.37mm and as shown in Fig. 8(b), in between depth of 1mm and 3mm, the compressive residual stress value for power density of 10 $GW\ cm^{-2}$ is always higher than that of 7 $GW\ cm^{-2}$. Moreover, comparing the depths of compressive residual stress for JC and EPP model which are roughly 1mm to 1.3mm with that for ZA model, we observed more than 100% increase in depths of compressive residual stress. As a result, higher plastic strain values in ZA model can be understood.

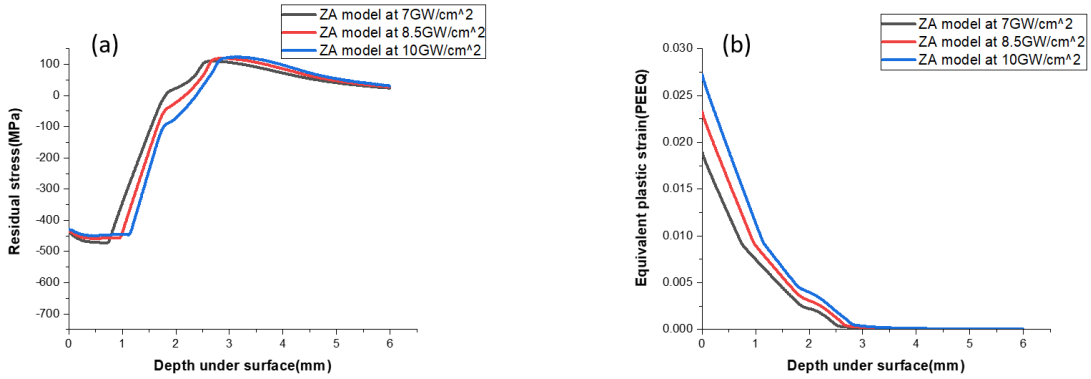

Fig.8: Simulation results for ZA model on (a) residual stress (b) PEEQ

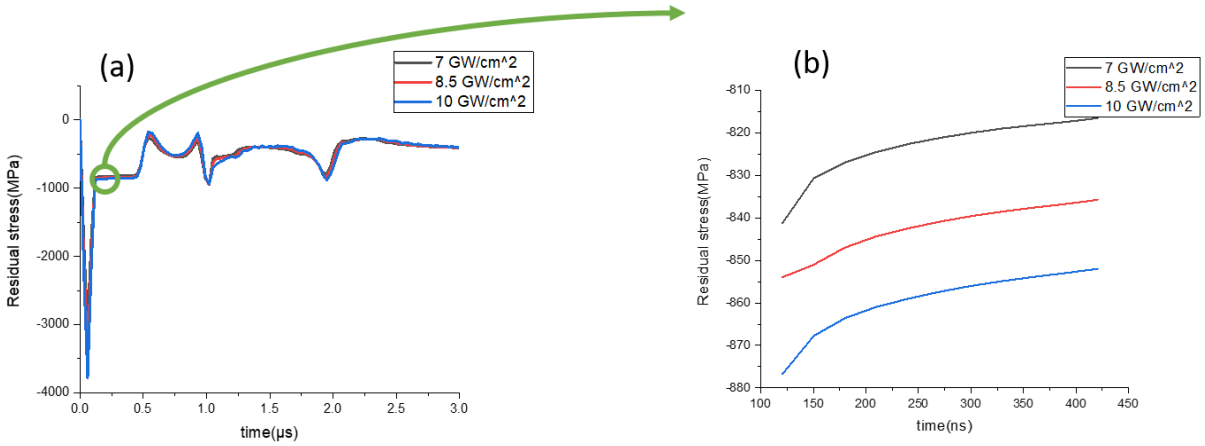

Fig.9: Time history of residual stress at x=1.4mm on surface (a) for 0<t<3μs (b) for 120ns<t<470ns

4.3 Enhanced ZA model

Fig. 10(a) and Fig. 10(b) shows the residual stress and equivalent plastic strain in enhanced ZA model versus depth below the surface curve for each power densities In Fig.5, the plastic strain for enhanced ZA model at 7 $GW\ cm^{-2}$ is close to 0 and as a result, in Fig.4, almost no compressive residual stress is induced in enhanced ZA model. It is obvious that enhanced ZA model requires a higher peak pressure in order to yield the material and the stress needed to yield the material is related to the yield stress of the material. According to Sun, R. et al[9], the stress after applying a pressure P can expressed as below:

$$\sigma = \frac{-P(1-2\nu)^2}{(1-\nu)+(1-2\nu)\sigma_y}$$

Where ν is the Poisson's ratio for desired material and σ_y is the yield stress of the material. Therefore, the threshold stress needed to yield the material is obtained by setting σ to zero. In our case, pressure required to yield Ti-lAl-4V is roughly 5.87GPa which is greater than 5.164GPa at 10 $GW\ cm^{-2}$.

In Fig.10 (b), the same trend for plastic strain as peak pressure increases still applies. However, even at 10 $GW\ cm^{-2}$, peak PEEQ value is only 0.0026 which is about a magnitude lower compared to other three models. This low plastic strain also affected residual stress as shown in Fig.10 (a). As a result, peak residual stress value for enhanced ZA model is much lower compared to other three models.

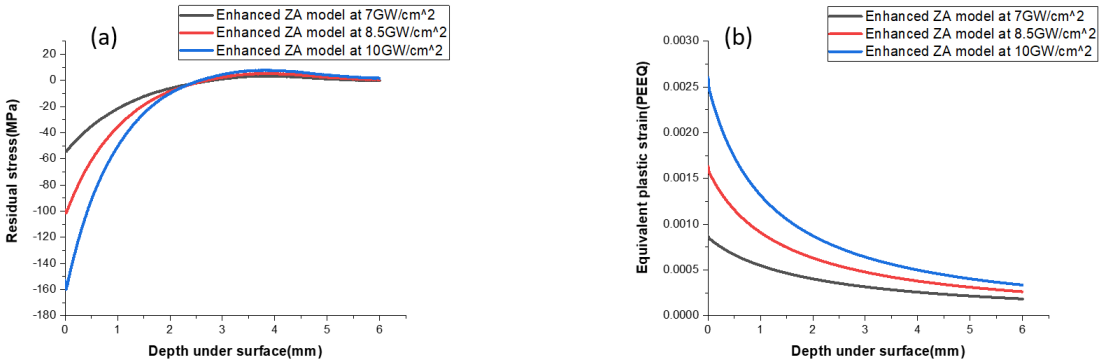

Fig.10: Simulation results for Enhanced ZA model on (a) residual stress (b) PEEQ

4.4 Other discussions

To better understand each model and further compare them, depth of compressive residual stress, maximum compressive residual stress and maximum tensile residual stress values were recorded and tabulated for each model as shown in table.2. All the data were collected at a distance of 1.4mm away from the center of the laser shot. JC model has slightly larger depth of compressive residual stress compared to EPP model and ZA model has the largest depth of compressive residual stress among 4

models. EPP model on the other hand predicts the highest compressive residual stress values among 4 models. Maximum tensile residual stress shows an increasing trend with increasing power density as expected.

Table.3 LSP performances for each model

Laser Intensity ($GW\ cm^{-2}$)	7				8.5				10			
Model	EPP	JC	ZA	Enhanced ZA	EPP	JC	ZA	Enhanced ZA	EPP	JC	ZA	Enhanced ZA
Depth of compressive residual stress(mm)	0.93	1.25	1.8	2.8	1.06	1.32	2.16	2.69	1.15	1.39	2.37	2.56
Maximum compressive residual stress (MPa)	-503.6	-490	-473	-54.5	-613.4	-593.8	-458	-101.3	-702.9	-683.8	-449.2	-159.9
Maximum tensile residual stress (MPa)	84	51.9	110.5	3.3	116.2	71	119.5	5.3	145.3	88.1	123.4	7.7

5. Experiments

5.1 Tensile tests and SEM on LSPed samples

Two sets of additive manufactured Ti6Al4V samples were shipped to and treated by LSP Technology Pte Ltd. One set of samples were treated by a 13ns laser at 10 $GW\ cm^{-2}$ power density without transparent overlay and absorbent coating. The other set of samples were treated by a 6ns laser at 7.5 $GW\ cm^{-2}$ power density with black tape as absorbent coating. Tensile testing was conducted perpendicular to the build direction of the sample with the maximum force of 2000N. During the testing process, camera was set up to take 2 frames per second and all the images were then processed through digital image correlation (DIC) to get the corresponding strain values. Testing results are shown in Fig.11. In Fig.11, as

built samples have slightly higher ultimate tensile strength and elongation compared with LSPed samples. Therefore, we did not observe the expected increase in ductility and ultimate tensile strength. One possible reason is insufficient pressure generated by LSP. Other researchers successfully performed LSP in air with femtosecond lasers[32]–[34] but for ns-LSP process, confining transparent overlay is required to generate sufficient pressure in order to plastically deform the material[35].

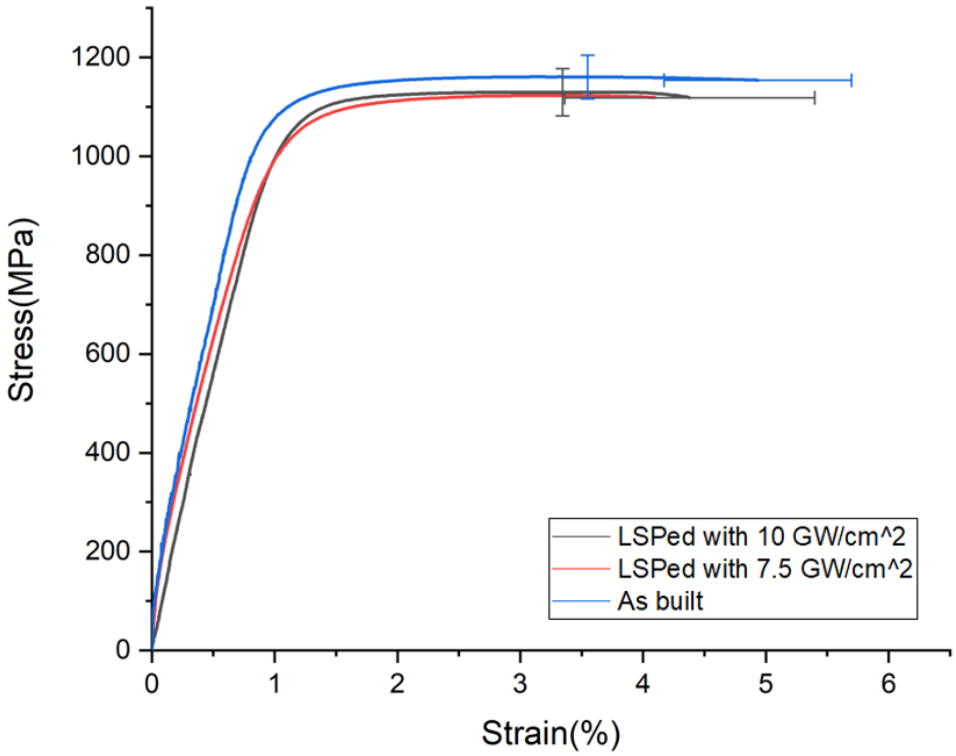

Fig.11: stress-strain curves of Ti6Al4V before and after LSP

Before doing the SEM, samples were grinded and polished to good quality and SEM was conducted on Tescan-Mira3-FESEM. Two magnifications were used in the images: x830 which was for general microstructure characterization and x4150 which was for detailed comparison. Three sets of SEM images before and after LSP images are shown in figure.12. The change in microstructure before and after LSP is minimal. We did not observe the expected change from needle-like α grains to equi-axed α grains due to

plastic deformation. This result further confirmed our hypothesis that pressure generated by LSP is insufficient to plastically deform our material.

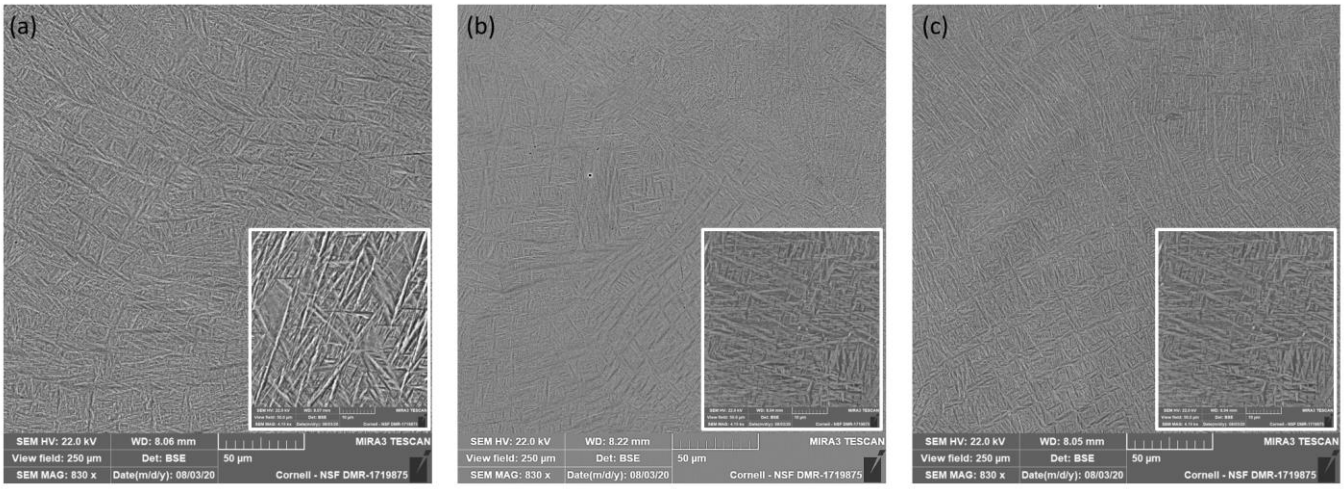

Fig.12: SEM images on (a) as built sample (b) LSPed sample at 7.5 $GW\ cm^{-2}$ (c) LSPed sample at 10 $GW\ cm^{-2}$

5.2 Electropolishing

In order to get residual stress data along depth, we decided to use electro polishing with lab scale XRD. A layer of material is removed during electropolishing process and XRD characterization of residual stress will be performed subsequently. Therefore, after repeating this process for many times, we are able to get residual stress data along depth.

Electropolishing process is a widely used process to create a smooth surface and for Ti-6Al-4V specifically, applied voltage of 55-80V and treatment time from 5mins to 20mins were reported[36], [37]. However, our goal is not to obtain a smooth surface but to evenly remove a layer of material. As a result, we need to figure out a suitable voltage and time for our purpose.

Our electropolishing setup is shown in Fig.12. Experiments was performed at 10V, 13V, 15V, 18V, 20V, 23V and 26V. At 10V-18V, the electropolishing effect is minimal even after 20mins. At 23V-26V, removal rate of material is very high and extremely uneven between edge region and center region.

Therefore, voltage should be set to about 20V to maintain a steady current flow of 0.1A so that a steady removal rate of 0.05mm in thickness per 5mins can be maintained. However, the removal rate is still uneven between edge region and center region. To solve this problem, wax was used to cover the edge region in the electropolishing process in order to create a flat surface. The total time needed to electropolish a sample from thickness of 1mm to 0.1mm is about 90mins and we will be able to get 20 data points along the process.

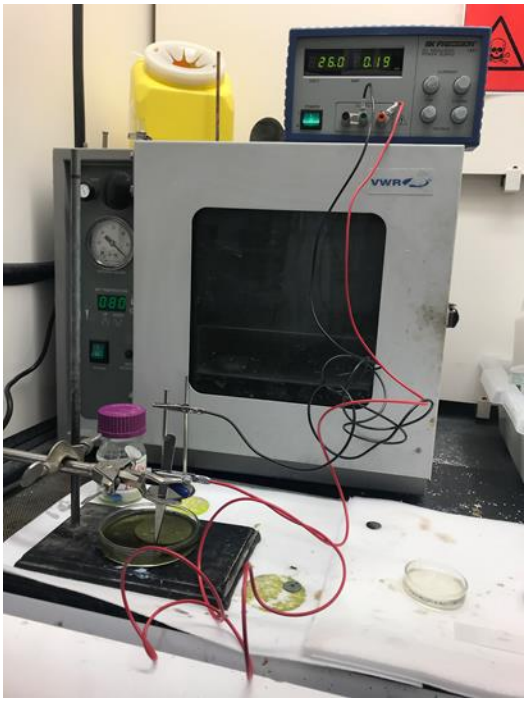

Fig.13: Electro polishing setup

6. Conclusion

In this work, different material models were used to simulate the process of LSP. Finite element analysis, Abaqus to be specific, is proven to be an accurate and useful tool for simulations. An accurate simulation based on valid models can be a guidance on experiments and theory crafting. Our simulation results showed that EPP model and JC model which are used extensively in simulations behaved similarly. On

the other hand, ZA model gave us the highest plastic strain and affected depth of LSP process. Enhanced ZA model, however, required a high power density of laser and as a result, showed low plastic strain and residual stress. A detailed comparison between all four models can be found below as Table.3. As for experiments, tensile tests and SEM images confirmed that induced pressure by LSP process in our case is not enough to plastically deform the material.

7. Future work

Since we still do not have experiment data for residual stress, first, we need to perform XRD experiment to get residual stress versus depth curve (possibly Synchrotron data to calculate residual stress and compare with data from lab scale XRD). If we find little to no compressive residual stress in the sample, then we need to either send more samples to the company and specifically request them to use water as transparent overlay or do the LSP process ourselves if we have a setup with a suitable pulse laser. If we actually find normal compressive residual stress in the sample, I still believe that we need to get more samples and characterize them again because residual stress data now contradicts tensile test results and SEM results.

As for simulation, another improvement is customized spatial distribution in Abaqus through VDLOAD user subroutine. If we can combine these two user subroutines, we will be able to create customized temporal and spatial profile that match the profiles of the laser. Afterwards, the final step would be data fitting for more accurate model parameters for each model using experiment data. Then, we can use the optimized parameters to do simulations with different power densities and compare simulation results with experiment results.

8. References

[1] S. Seo, O. Min, and H. Yang, "Constitutive equation for Ti-6Al-4V at high temperatures measured using the SHPB technique," *Int. J. Impact Eng.*, vol. 31, no. 6, pp. 735–754, Jul. 2005, doi: 10.1016/j.ijimpeng.2004.04.010.

[2] Q. Xue, M. A. Meyers, and V. F. Nesterenko, "Self-organization of shear bands in titanium and Ti-6Al-4V alloy," *Acta Mater.*, vol. 50, no. 3, pp. 575–596, Feb. 2002, doi: 10.1016/S1359-6454(01)00356-1.

[3] H. K. Amarchinta, R. V. Grandhi, A. H. Clauer, K. Langer, and D. S. Stargel, "Simulation of residual stress induced by a laser peening process through inverse optimization of material models," *J. Mater. Process. Technol.*, vol. 210, no. 14, pp. 1997–2006, Nov. 2010, doi: 10.1016/j.jmatprotec.2010.07.015.

[4] C. S. Montross, T. Wei, L. Ye, G. Clark, and Y. W. Mai, "Laser shock processing and its effects on microstructure and properties of metal alloys: A review," *Int. J. Fatigue*, vol. 24, no. 10, pp. 1021–1036, 2002, doi: 10.1016/S0142-1123(02)00022-1.

[5] B. P. Fairand, A. H. Clauer, R. G. Jung, and B. A. Wilcox, "Quantitative assessment of laser-induced stress waves generated at confined surfaces," *Appl. Phys. Lett.*, vol. 25, no. 8, pp. 431–433, 1974, doi: 10.1063/1.1655536.

[6] J. D. O'Keefe and C. H. Skeen, "Laser-induced stress-wave and impulse augmentation," *Appl. Phys. Lett.*, vol. 21, no. 10, pp. 464–466, 1972, doi: 10.1063/1.1654220.

[7] C. G. Hoffman, "Laser-target interactions," *J. Appl. Phys.*, vol. 45, no. 5, pp. 2125–2128, 1974, doi: 10.1063/1.1663556.

[8] L. C. Yang, "Stress waves generated in thin metallic films by a Q -switched ruby laser," *J. Appl. Phys.*, vol. 45, no. 6, pp. 2601–2608, 1974, doi: 10.1063/1.1663636.

[9] R. Sun *et al.*, "Dynamic response and residual stress fields of Ti6Al4V alloy under shock wave induced by laser shock peening," *Model. Simul. Mater. Sci. Eng.*, vol. 25, no. 6, Jul. 2017, doi: 10.1088/1361-651X/aa7a46.

[10] R. Sun *et al.*, "Microstructure, residual stress and tensile properties control of wire-arc additive manufactured 2319 aluminum alloy with laser shock peening," *J. Alloys Compd.*, vol. 747, pp. 255–265, May 2018, doi: 10.1016/j.jallcom.2018.02.353.

[11] L. Berthe, R. Fabbro, P. Peyre, L. Tollier, and E. Bartnicki, "Shock waves from a water-confined laser-generated plasma ARTICLES YOU MAY BE INTERESTED IN," *J. Appl. Phys.*, vol. 82, p. 2826, 1997, doi: 10.1063/1.366113.

[12] X. Wu, C. Huang, X. Wang, and H. Song, "A new effective method to estimate the effect of laser shock peening," *Int. J. Impact Eng.*, vol. 38, no. 5, pp. 322–329, May 2011, doi: 10.1016/j.ijimpeng.2010.11.008.

[13] D. Grevey, L. Maiffredy, and A. B. Vannes, "Laser shock on a TRIP alloy: mechanical and metallurgical consequences," *J. Mater. Sci.*, vol. 27, no. 8, pp. 2110–2116, Apr. 1992, doi: 10.1007/BF01117924.

[14] Z. Hong and Y. Chengye, "Laser shock processing of 2024-T62 aluminum alloy," *Mater. Sci. Eng. A*, vol. 257, no. 2, pp. 322–327, Dec. 1998, doi: 10.1016/S0921-5093(98)00793-X.

[15] W. Braisted and R. Brockman, “Finite element simulation of laser shock peening,” *Int. J. Fatigue*, vol. 21, no. 7, pp. 719–724, Aug. 1999, doi: 10.1016/S0142-1123(99)00035-3.

[16] A. F. M. Arif, “Numerical prediction of plastic deformation and residual stresses induced by laser shock processing,” *J. Mater. Process. Technol.*, vol. 136, no. 1–3, pp. 120–138, May 2003, doi: 10.1016/S0924-0136(02)01122-6.

[17] B. Wu and Y. C. Shin, “A simple model for high fluence ultra-short pulsed laser metal ablation,” 2006, doi: 10.1016/j.apsusc.2006.09.007.

[18] S. Laville *et al.*, “Fluid modeling of the laser ablation depth as a function of the pulse duration for conductors,” doi: 10.1103/PhysRevE.66.066415.

[19] M. A. Meyers, *Dynamic Behavior of Materials*. New York: John Wiley & Sons, 1994.

[20] G. Bae, Y. Xiong, S. Kumar, K. Kang, and C. Lee, “General aspects of interface bonding in kinetic sprayed coatings,” *Acta Mater.*, vol. 56, no. 17, pp. 4858–4868, Oct. 2008, doi: 10.1016/j.actamat.2008.06.003.

[21] F. J. Zerilli and R. W. Armstrong, “Dislocation-mechanics-based constitutive relations for material dynamics calculations,” *J. Appl. Phys.*, vol. 61, no. 5, pp. 1816–1825, Mar. 1987, doi: 10.1063/1.338024.

[22] R. W. Zerilli, F. J., and Armstrong, “Shock Compression of Condensed Matter,” in *AIP Conference Proceedings (No. 370)*, 1995, pp. 31–35.

[23] H. K. Amarchinta, R. V. Grandhi, K. Langer, and D. S. Stargel, “Material model validation for laser shock peening process simulation,” *Model. Simul. Mater. Sci. Eng.*, vol. 17, no. 1, p. 015010, Dec. 2009, doi: 10.1088/0965-0393/17/1/015010.

[24] Y. Liao, C. Ye, and G. J. Cheng, “[INVITED] A review: Warm laser shock peening and related laser processing technique,” *Opt. Laser Technol.*, vol. 78, pp. 15–24, Apr. 2016, doi: 10.1016/j.optlastec.2015.09.014.

[25] “Abaqus Version 6.7 Documentation.” http://130.149.89.49:2080/v6.7/index.html (accessed Dec. 03, 2020).

[26] Ding K and Ye L, *Laser Shock Peening: Performance and Process Simulation*. Cambridge: Woodhead Publishing Limited, 2006.

[27] H. K. Amarchinta, R. V. Grandhi, K. Langer, and D. S. Stargel, “Material model validation for laser shock peening process simulation,” *Model. Simul. Mater. Sci. Eng.*, vol. 17, no. 1, p. 015010, Dec. 2009, doi: 10.1088/0965-0393/17/1/015010.

[28] R. Fabbro, P. Peyre, L. Berthe, and X. Scherpereel, “Physics and applications of laser-shock processing,” *J. Laser Appl.*, vol. 10, no. 6, pp. 265–279, Dec. 1998, doi: 10.2351/1.521861.

[29] P. Peyre, R. Fabbro, P. Merrien, and H. P. Lieurade, “Laser shock processing of aluminium alloys. Application to high cycle fatigue behaviour,” *Mater. Sci. Eng. A*, vol. 210, no. 1–2, pp. 102–113, Jun. 1996, doi: 10.1016/0921-5093(95)10084-9.

[30] K. Ding and L. Ye, “Simulation of multiple laser shock peening of a 35CD4 steel alloy,” *J. Mater. Process. Technol.*, vol. 178, no. 1–3, pp. 162–169, Sep. 2006, doi: 10.1016/j.jmatprotec.2006.03.170.

[31] R. Sun *et al.*, “Dynamic response and residual stress fields of Ti6Al4V alloy under shock wave induced by laser shock peening,” *Model. Simul. Mater. Sci. Eng.*, vol. 25, no. 6, p. 065016, Jul.

2017, doi: 10.1088/1361-651X/aa7a46.

[32] H. Wang *et al.*, “Corrosion behavior of NiTi alloy subjected to femtosecond laser shock peening without protective coating in air environment,” *Appl. Surf. Sci.*, vol. 501, p. 144338, Jan. 2020, doi: 10.1016/j.apsusc.2019.144338.

[33] Y. Li *et al.*, “The effects of the confining medium and protective layer during femtosecond laser shock peening,” *Manuf. Lett.*, vol. 27, pp. 26–30, Jan. 2021, doi: 10.1016/j.mfglet.2020.11.006.

[34] “Femtosecond laser peening of 2024 aluminum alloy without a sacrificial overlay under atmospheric conditions,” *J. Laser Appl.*, vol. 29, no. 1, p. 012005, Feb. 2017, doi: 10.2351/1.4967013.

[35] U. Trdan, T. Sano, D. Klobčar, Y. Sano, J. Grum, and R. Šturm, “Improvement of corrosion resistance of AA2024-T3 using femtosecond laser peening without protective and confining medium,” *Corros. Sci.*, vol. 143, pp. 46–55, Oct. 2018, doi: 10.1016/j.corsci.2018.08.030.

[36] L. Yang, H. Gu, and A. Lassell, “Surface treatment of Ti6Al4V parts made by powder bed fusion additive manufacturing processes using electropolishing.”

[37] L. Yang, A. Lassell, G. Perez, and V. Paiva, “Further study of the electropolishing of Ti6Al4V parts made via electron beam melting.”